

Crystallization, phase evolution and corrosion of Fe-based metallic glasses: An atomic-scale structural and chemical characterization study

M.J. Duarte^{a,b,*}, A. Kostka^b, J.A. Jimenez^c, P. Choi^b, J. Klemm^a, D. Crespo^d,
D. Raabe^b, F.U. Renner^{a,e}

^a Department of Interface Chemistry and Surface Engineering, Max-Planck Institut für Eisenforschung GmbH, 40237 Düsseldorf, Germany

^b Department of Microstructure Physics and Alloy Design, Max-Planck Institut für Eisenforschung GmbH, 40237 Düsseldorf, Germany

^c CENIM-CSIC, Avda. Gregorio del Amo 8, 28040 Madrid, Spain

^d Departament de Física Aplicada, Universitat Politècnica de Catalunya, 08860 Castelldefels, Spain

^e Instituut Voor Materiaalonderzoek, Universiteit Hasselt, 3590 Diepenbeek, Belgium

Received 15 January 2014; received in revised form 19 February 2014; accepted 19 February 2014

Abstract

Understanding phase changes, including their formation and evolution, is critical for the performance of functional as well as structural materials. We analyze in detail microstructural and chemical transformations of the amorphous steel $\text{Fe}_{50}\text{Cr}_{15}\text{Mo}_{14}\text{C}_{15}\text{B}_6$ during isothermal treatments at temperatures ranging from 550 to 800 °C. By combining high-resolution transmission electron microscopy and Rietveld analyses of X-ray diffraction patterns together with the local chemical data obtained by atom probe tomography, this research provides relevant information at the atomic scale about the mechanisms of crystallization and the subsequent phases evolution. During the initial stages of crystallization a stable $(\text{Fe,Cr})_{23}(\text{C,B})_6$ precipitates as well as two metastable intermediates of $\text{M}_3(\text{C,B})$ and the intermetallic χ -phase. When full crystallization is reached, only a percolated nano-scale Cr-rich $(\text{Fe,Cr})_{23}(\text{C,B})_6$ and Mo-rich $\eta\text{-Fe}_3\text{Mo}_3\text{C}$ structure is detected, with no evidence to suggest that other phases appear at any subsequent time. Finally, the corrosion behavior of the developed phases is discussed from considerations of the obtained atomic information.

© 2014 Acta Materialia Inc. Published by Elsevier Ltd. All rights reserved.

Keywords: Metallic glasses; Crystallization; Phase evolution; Atom probe tomography; Transmission electron microscopy

1. Introduction

The microstructure and performance of materials are strongly linked to each other, hence understanding transformations such as precipitation or crystallization is essential for advanced materials design. The production of amorphous/crystalline composites (ACCs) or fully crystalline alloys from metastable metallic glasses by controlled

crystallization presents a broad potential in the processing or improvement of new materials and nanostructures. Crystallization towards ACCs or fully (nano-)crystalline states determines the transition away from the original properties of the amorphous alloy [1,2] since mechanical [3], magnetic [4] or chemical [5] properties critically depend on this specific structural state. For example, the precipitation of isolated crystalline particles below 50 nm size enhances the properties of Fe-based soft magnetic alloys [6–8]. Even in the amorphous state, embrittlement is induced after annealing close to the glass transition temperature, which has been associated to structural relaxation

* Corresponding author at: Max-Planck Institut für Eisenforschung GmbH, 40237 Düsseldorf, Germany.

E-mail address: j.duarte@mpie.de (M.J. Duarte).

effects [9]. Also, as recently reported by our group, the often very good corrosion resistance of Fe-based metallic glasses may be compromised after partial or complete alloy crystallization [10]. Therefore, the characterization and understanding of microstructural changes during the devitrification process and their relationship with the performance of the alloy are key issues to design new functional materials with a tailored microstructure [6–8,11] or to avoid the unwanted deterioration of the compound's original properties [11,12].

Among metallic glasses, bulk Fe-based amorphous alloys [13], also referred as amorphous steels, have drawn special interest, for instance owing to their excellent soft magnetic properties [6–8,14]. In addition to the quest for higher glass forming ability, soft magnetic properties, fracture strength [15] and corrosion resistance [16], recent developments allowed the preparation of amorphous steels at low cost by using industrial ferrous alloys [17], making them suitable also as structural materials. Metallic glasses are unstable at high temperatures and they may form intermediate metastable phases as the temperature rises to finally crystallize to stable structures. Hence, to have detailed information for predicting and controlling the crystallization process to achieve the optimum microstructure for a specific property is essential. Published studies deal with kinetics of crystallization or the effects of annealing on specific properties. Few of these works follow the full crystallization process, mainly by X-ray diffraction (XRD) [14]. However, there is a clear lack of detailed evidence on the changes of the local chemical or compositional states of the occurring phases during de-vitrification.

With transmission electron microscopy (TEM) the local structure of a material is experimentally accessible, even at small length scales. The local, near-atomic-scale chemical composition is, in contrast, much harder to quantify. Atom probe tomography (APT) provides atom-by-atom three-dimensional chemical information with sub-nm localization and has grown into a widely available method [18,19]. In particular, for nano-scale morphologies such as nanocrystalline materials and interfaces, the high-resolution chemical information provided by APT becomes an important tool for understanding materials performance such as mechanical or corrosion behavior [20–24].

We present here a detailed study of the crystallization and phase evolution of the $\text{Fe}_{50}\text{Cr}_{15}\text{Mo}_{14}\text{C}_{15}\text{B}_6$ [25] amorphous alloy. The structural characteristics are obtained by TEM and XRD, while APT provides the associated chemical information. Finally, an insight into corrosion properties is presented in correlation with the observed microstructural and chemical changes of the alloy.

2. Experimental

Amorphous ribbons 2–3 mm in width and $\sim 40\ \mu\text{m}$ in thickness of nominal composition $\text{Fe}_{50}\text{Cr}_{15}\text{Mo}_{14}\text{C}_{15}\text{B}_6$ (all compositions given in this paper are in at.%) were produced by melt spinning at a speed of $40\ \text{m s}^{-1}$ [26,27] in a

Melt Spinner SC from Edmund Bühler GmbH. The master alloy was prepared by arc melting the constituent metals with purity greater than 99.9% in a purified Ti-gettered argon atmosphere.

Phase transformations were monitored as changes in heat flow by differential scanning calorimetry (DSC) in a NETZSCH 404F3 instrument at a heating rate of $0.33\ ^\circ\text{C s}^{-1}$. Thermal annealing was carried out inside quartz tubes with Ar atmosphere at 550, 610, 620, 650, 670, 720 and $800\ ^\circ\text{C}$ for 20 min, in a furnace from Heraeus Instruments. After annealing, the specimens were taken out of the furnace and cooled at room temperature.

TEM specimens were prepared using a Gatan Precision Ion Polishing System 691 (PIPS) operated at 5 kV. Additional samples, not included here, were prepared from the amorphous and the fully crystallized alloys near the edge of the ribbon, by focused ion beam, showing a similar behavior as the central part prepared by PIPS. TEM was performed using a JEOL JEM-2200FS operated at 200 kV. Images with a high atomic number contrast were acquired using a high angle annular dark field (HAADF) detector in scanning mode (STEM). Average grain size values were calculated from the STEM images using a statistical analysis over more than 200 grains measured for each annealing temperature.

XRD measurements were carried out in a Bruker AXS diffractometer equipped with an X-ray Cu tube ($\text{Cu K}\alpha$, $\lambda = 0.1541\ \text{nm}$). XRD patterns were collected over a 2θ range from 20° to 110° with a step width of 0.05° and a counting time of 5 s per step. Phase identification was done using the JCPDS database and the DIFFRACplus EVA software by Bruker AXS. Quantitative phase-composition analyses by the Rietveld method were used for the XRD data refinement with the version 4.2 of the Rietveld analysis program TOPAS (Bruker AXS). As X-ray powder diffraction is sensitive only to crystalline materials, any amorphous component of a sample is not considered and included in the background of the Rietveld analysis. The pseudo-amorphous approximation was then used to model the contribution of the amorphous part of the sample in the refinement [28]. The amorphous phase was considered then as a crystalline one by using the crystallographic information of the cubic $\text{M}_{23}(\text{C},\text{B})_6$ [29], and decreasing the crystallite size down to $\sim 1\ \text{nm}$.

The crystalline structures used in the Rietveld refinement and TEM diffraction analyses were an appropriated combination of the carbide M_6C , the borocarbides $\text{M}_{23}(\text{C},\text{B})_6$ and $\text{M}_3(\text{C},\text{B})$, and a ternary Fe–Cr–Mo intermetallic. The M_6C carbide ($\eta\text{-Fe}_3\text{Mo}_3\text{C}$), generally referred as η -carbide, is a face centered cubic structure (space group $Fd\text{-}3m$) with 112 atoms in the unit cell [30]. $\text{M}_{23}(\text{C},\text{B})_6$ crystallizes in a cubic face-centered structure (space group $Fm\text{-}3m$) [29] while $\text{M}_3(\text{C},\text{B})$ corresponds to the orthogonally system (space group $Pnma$) [31]. The ternary χ -phase, also called τ_1 phase [32], is a considerably non-stoichiometric intermetallic compound of proposed composition $\text{Cr}_6\text{Fe}_{18}\text{Mo}_5$. The χ -phase crystallizes in a body centered cubic

(bcc) system similar to α -Mn (space group $I4-3m$). The unit cell consists of 58 atoms distributed on four sublattices with 2, 8, 24 and 24 atoms on each. One of the 24 atom sublattice has a tetrahedrally coordinated shell with 13 neighbors, which distinguishes the χ -phase from other topologically close-packed phases [33,34].

APT measurements were performed using a local electrode atom probe, Imago LEAP™ 3000X HR in voltage mode at 200 kHz pulse frequency, with a pulse fraction of 15%, a detection rate of 0.5% and a specimen base temperature set to 60 K. The specimens were prepared using a FEI Helios Nanolab 600 dual-beam focused ion beam system as described in Refs. [35,36]. A final milling of the tip was done at low ion energies of 5 kV to minimize Ga implantation. To ensure reproducibility of the data, different regions from different samples were prepared, including thin needle shaped by-products of the ribbons. The reconstructed tips show a negligible Ga content in the regions of interest. A distribution analysis for every element in the alloy in the amorphous state was performed. The statistical analysis is made by using the chi-square distribution that measures the divergence of the observed data from the values that would be expected in a binomial distribution. The chi-square distribution with k degrees of freedom is the distribution of a sum of the squares of the X_i , k independent and normally distributed random variables, with means μ_i and standard deviation σ_i , and its expression can be reduced as: $\chi^2 = \sum_{i=1}^k \left(\frac{X_i - \mu_i}{\sigma_i} \right)^2$. A low reduced chi-square value indicates a high probability of a normal distribution, meaning that the elements are distributed randomly. The chi-square distribution is associated with the P -value, which is a measure of how much evidence there is to reject a result of the data set. A P -value of 0.05 or less is usually regarded as statistically significant. Additionally, an iterative process based on iso-concentration surfaces was used to evaluate the composition of the different phases formed in the annealed samples. The regions of interest were clipped and isolated to analyze their respective mass spectra. Proximity histograms were calculated to generate concentration profiles across the selected interfaces [37]. Finally, cylindrical regions were cut out from the full reconstructions for better visual clarity.

Electrochemical measurements using a scanning droplet cell were performed in a capillary three-electrode setup with a gold counter electrode and a micro Ag|AgCl reference electrode [38]. The diameter of the circular wetted area was $374 \mu\text{m}^2$. The open circuit potential was stabilized for 100 s in aerated 0.1 M HCl aqueous solution followed by linear polarization in the positive direction starting at 0.3 V with a potential scan rate of 2 mV s^{-1} at ambient pressure and temperature. All potentials were referred to the standard hydrogen electrode (SHE). Additional galvanostatic polarization was performed on amorphous and annealed samples close to the breakdown potential for 2000 s. Prior to the electrochemical tests, all the samples were ion milled for 5 min at a tilting angle of 70° to remove

the surface oxide layer, in a Gatan 682 Precision Etching Coating System (PECS) with argon ions at 5 keV. Suprapure HCl was used to prepare the acid electrolytes, while Cr and Mo foils, used for comparison, were obtained from Goodfellow with a purity higher than 99.99%.

Sample cross-sections were observed in a field emission scanning electron microscope (FE-SEM), Leo 1550 VP. The cuts were made in a cross-section polisher (Hitachi IM4000) using a beam energy of 6 keV and swing angle of $\pm 30^\circ$.

3. Results

3.1. Microstructure

The characteristics of the $\text{Fe}_{50}\text{Cr}_{15}\text{Mo}_{14}\text{C}_{15}\text{B}_6$ as-spun ribbons are summarized in Fig. 1. The X-ray and electron diffraction patterns, Fig. 1a and c, show broad and diffuse peaks, characteristic of an amorphous state. The homogeneity of the microstructure through the sample is evidenced by the absence of nanometer-sized structures (clusters or grains) in the bright-field (BF) STEM image, Fig. 1b, and the uniform elemental distribution in the selected cylinder reconstruction, Fig. 1d. Here, the individual atoms are

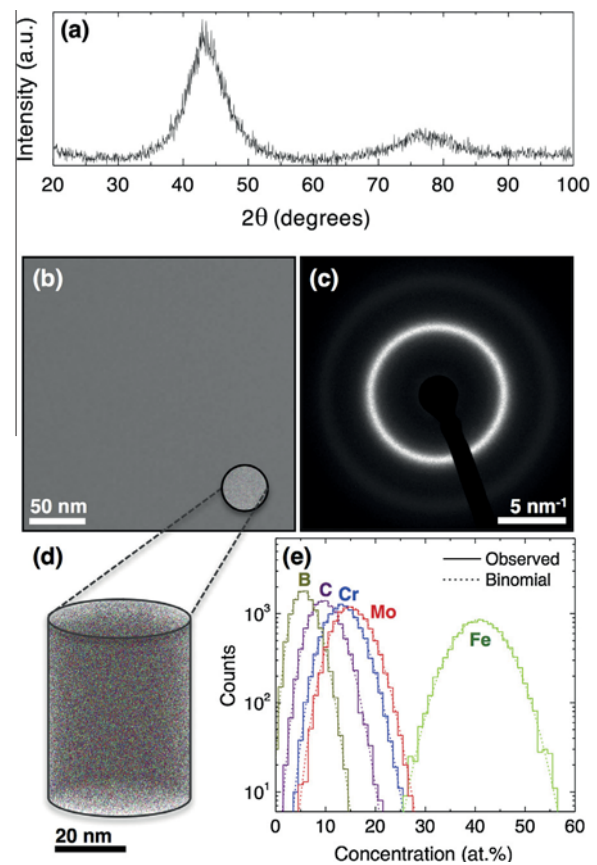


Fig. 1. As-quenched $\text{Fe}_{50}\text{Cr}_{15}\text{Mo}_{14}\text{C}_{15}\text{B}_6$ sample. (a) XRD pattern, (b) bright-field STEM image, (c) selected area electron diffraction pattern, (d) APT reconstruction showing the elemental distribution of a cylindrical selection and (e) distribution analysis of the full reconstructed volume showing a random (binomial) elemental distribution.

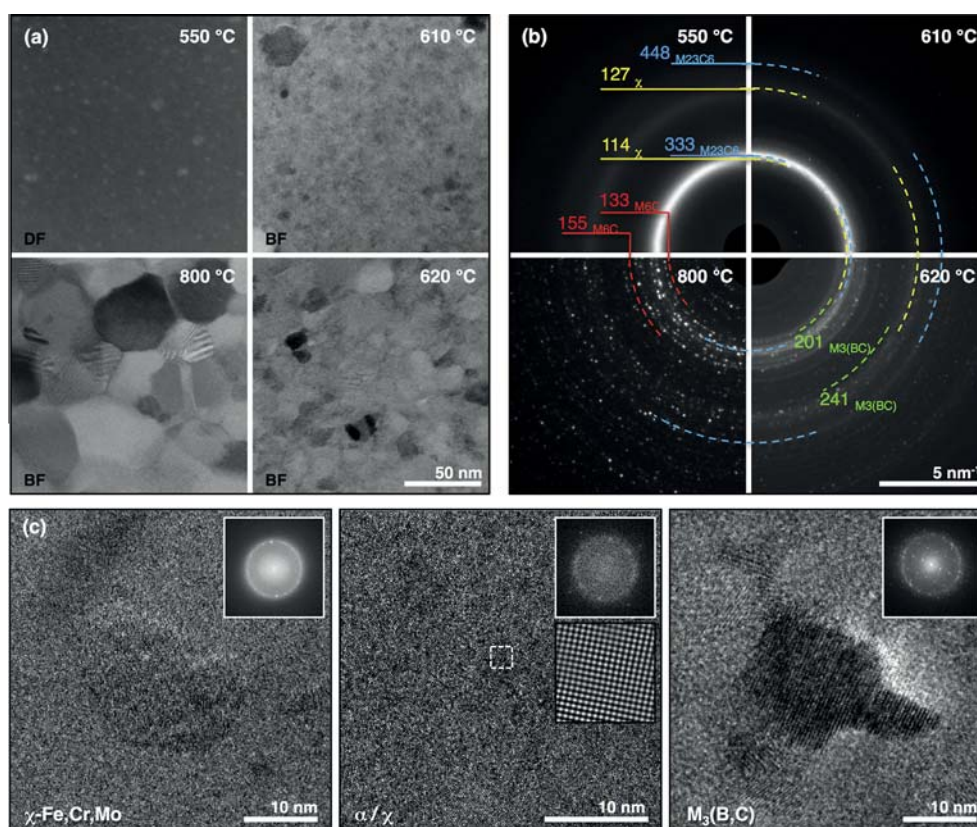


Fig. 2. (a) HAADF (550 °C) and BF-STEM (610, 620 and 800 °C) images and (b) selected area diffractions of the $\text{Fe}_{50}\text{Cr}_{15}\text{Mo}_{14}\text{C}_{15}\text{B}_6$ alloys annealed at 550, 610, 620 and 800 °C. (c) HR-TEM and corresponding FFT from the intermediate phases formed during crystallization.

mapped as colored dots:¹ green for Fe, blue for Cr, red for Mo, purple for C and yellow for B. A fully homogeneous amorphous state is also quantitatively supported by the distribution analysis shown in Fig. 1e, where the experimental distribution follows a binomial form. The confidence chi-square values were close to the unity with large *P*-values for the statistical calculations, indicating a perfectly random mix of the elements. The average bulk composition calculated from the APT mass spectra is 46.3% Fe, 15.3% Cr, 17.4% Mo, 14.3% C and 6.8% B. Although the general composition is close to the nominal one, some deviations are observed mainly due to an over-quantification of Mo and B, with a consequent decrease in the Fe concentration. These deviations were possibly related to the different evaporation fields of the individual elements within the alloy, leading to preferential field evaporation or retention, peak overlaps in the mass spectra and a high number of multiple events at the detector. After determining the optimum experimental parameters, they were used for all the samples to allow reproducibility and consistency in the chemical quantification of the different sample states.

DSC analyses served as an indicator of the transformations undergone by the alloy during heating. At a heating

rate of $0.33\text{ }^{\circ}\text{C s}^{-1}$ the measured glass transition temperature was $T_g = 550\text{ }^{\circ}\text{C}$, the onset of the first and second crystallization temperatures were $T_{x1} = 602\text{ }^{\circ}\text{C}$, $T_{x2} = 641\text{ }^{\circ}\text{C}$ and the melting temperature $T_m = 1112\text{ }^{\circ}\text{C}$. Crystallization of the amorphous ribbons was then induced by thermal annealing close to these values.

Selected TEM results in Fig. 2 exemplify different crystallization stages after heat treatments at 550, 610, 620 and 800 °C for 20 min. Annealing close to the glass transition temperature ($T_g = 550\text{ }^{\circ}\text{C}$) generates chemical segregation that is visible as contrast variations in the HAADF STEM image (Fig. 2a). Here, the atomic contrast highlights regions of $\sim 3\text{ nm}$ in diameter and a few larger ones of $\sim 9\text{ nm}$. However, this observed chemical heterogeneity is not yet related to crystallization as deduced by the corresponding diffuse rings in the selected area diffraction pattern (Fig. 2b). After annealing above the first crystallization temperature, $T_{x1} = 602\text{ }^{\circ}\text{C}$, the resulting microstructure is a multiphase composite formed by different crystalline phases embedded in an amorphous matrix. At 610 °C two crystalline signatures emerge from the amorphous rings. The diffraction patterns at this temperature can be assigned to the ternary intermetallic Fe–Cr–Mo, known as χ phase (identified by the (114) and (127) crystallographic planes as yellow dotted rings in Fig. 2b), and a $(\text{Fe,Cr})_{23}(\text{C,B})_6$ carbide (blue dotted rings corresponding to the (333) and (448) planes). Grains of two different sizes

¹ For interpretation of color in Figs. 1 and 2, the reader is referred to the web version of this article.

Table 1

Grain size calculated by the Rietveld method from the XRD patterns and measured from the STEM images after annealing. The numbers in parentheses stand for the uncertainty on the last significant digit and the standard deviation for the grain size calculations by Rietveld and TEM analyses, respectively.

Phase	610 °C	620 °C	650 °C	670 °C	720 °C	800 °C
<i>Grain size (nm) calculated by the Rietveld method from the XRD data</i>						
χ	14(5)	14(5)	12(2)	—	—	—
$(\text{Fe,Cr})_{23}(\text{C,B})_6$	5(1)	8(3)	10(2)	13(4)	17(3)	33(5)
$\text{M}_3(\text{C,B})$	—	13(5)	13(6)	—	—	—
$\eta\text{-Fe}_3\text{Mo}_3\text{C}$	—	—	8(2)	11(3)	11(2)	27(5)
	610 °C	620 °C	650 °C	800 °C	900 °C	
<i>Grain size (nm) measured from the STEM images</i>						
Size range ^a	2–30	2–30	2–33	3–56	3–220	
Small particles ^b	5.2(2.1)	9.6(4.4)	10.4(5.1)	8.1(1.9)	8.8(3.9)	
Large particles ^c	15.4(5.2)	25.0(5.7)	24.6(3.8)	35.7(12.2)	89.3(33.3)	

^a Smallest and largest values measured.

^{b,c} Average size of the small and large particles determined by the statistical analysis over all the measured grains.

are observed in the corresponding bright-field STEM image. A summary of the grain size as measured from the STEM images is presented in Table 1. Small grains have an average size of 4.4 nm while the larger grains can grow up to 30 nm. These two phases continue growing at 620 °C, where the smaller particles reach an average size of ~10 nm. At the same temperature, a new $\text{M}_3(\text{C,B})$ borocarbide phase appears, as indicated by the green dotted rings corresponding to the (201) and (241) planes in the diffraction pattern. The amorphous halo is still observed here as a background signal. At 800 °C no traces of the amorphous background were left. Large grains up to 56 nm were observed with smaller particles up to 10 nm embedded in some cases inside the larger grains. Only two phases remain stable at this temperature, the $(\text{Fe,Cr})_{23}(\text{C,B})_6$ carbide and an $\eta\text{-Fe}_3\text{Mo}_3\text{C}$ phase (red dotted rings of the (133) and (155) planes).

Structural phase identification may be especially confusing as several signatures in the diffraction pattern overlap for grains with similar crystallography. To confirm the identified phases, high-resolution (HR) TEM analyses were performed over several well oriented crystals. While the main stable phases, $\text{M}_{23}(\text{B,C})_6$ and $\eta\text{-Fe}_3\text{Mo}_3\text{C}$, can be easily identified by several experimental techniques, this is not the case of the intermediate metastable phases. The lower panels (c) of Fig. 2 show high-resolution (HR) TEM images of the intermediate phases found at the lower annealing temperatures of 610 and 620 °C. The insets present the corresponding fast Fourier transforms (FFTs) of the structures used to match the observed patterns: χ , $\alpha\text{-Fe}$ solid solution and $\text{M}_3(\text{C,B})$ phases. Note that the middle image was named α/χ , as the main diffracted plains correspond to an α , bcc, solid solution; however, the structure cannot be unambiguously resolved. As the intensity of the signal is low, there is still a possibility that the signatures of the χ -phase superlattice are imperceptible due to the high background.

In addition, XRD is a powerful tool for quantitative phase-composition analysis when the Rietveld method is used for data refinement. X-ray diffractograms and the corresponding Rietveld analysis of the crystallized samples are

presented in Fig. 3. After annealing at 610 °C, the XRD pattern refinement shows a composite structure of two crystalline phases, $(\text{Fe,Cr})_{23}(\text{C,B})_6$ and the intermetallic χ -phase in an amorphous matrix. Although a Rietveld fit using a bcc $\text{Cr}(\text{Mo})$ solid solution instead of the χ -phase

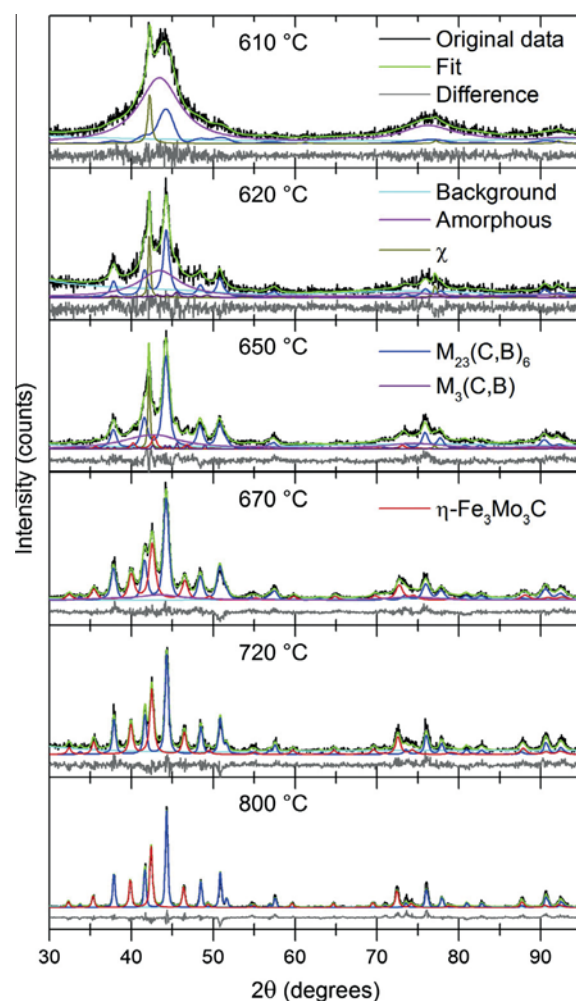


Fig. 3. Rietveld analyses of XRD patterns of the $\text{Fe}_{50}\text{Cr}_{15}\text{Mo}_{14}\text{C}_{15}\text{B}_6$ alloy after annealing at different temperatures for 20 min.

is also satisfactory, this last one was chosen in correlation with the TEM and APT results. Besides, the ternary Fe–Cr–Mo phase diagram predicts the presence of the intermetallic χ -phase for an alloy with the composition close to $\text{Fe}_{50}\text{Cr}_{15}\text{Mo}_{14}$ [32]. A third phase identified as $\text{M}_3(\text{C},\text{B})$ appears after annealing at 620 °C and finally, the $\eta\text{-Fe}_3\text{Mo}_3\text{C}$ is detected above 670 °C. The $\text{M}_3(\text{C},\text{B})$ and χ phases are intermediate phases and they transform or dissolve over 650 °C. $(\text{Fe,Cr})_{23}(\text{C},\text{B})_6$ and $\eta\text{-Fe}_3\text{Mo}_3\text{C}$ remain stable until the crystallization is completed, with no evidence to suggest that other phases appear at any subsequent time.

The temperature ranges at which each phase is stable are better visualized in Fig. 4, where the phase mass fraction is plotted against the annealing temperature. In the figure, the section of the bar chart required to sum 100% corresponds to the remaining amorphous phase after annealing at temperatures below 720 °C. The dominant phase at each studied temperature is $(\text{Fe,Cr})_{23}(\text{C},\text{B})_6$, constituting up to 70–76% of the crystallized material. The only analyzed temperature at which all phases coexist is 650 °C. The formation of the $\eta\text{-Fe}_3\text{Mo}_3\text{C}$ carbide is then linked to the transformation and disappearance of the intermediate phases. Full crystallization is achieved at ~ 720 °C and the microstructure of the alloy above this temperature is composed only by the two $(\text{Fe,Cr})_{23}(\text{C},\text{B})_6$ and $\eta\text{-Fe}_3\text{Mo}_3\text{C}$ carbides in a ratio of 7:3, respectively.

Grain size and lattice parameters calculated by the Rietveld method are presented in Tables 1 and 2, respectively. The larger changes in the grain growth are observed for the $(\text{Fe,Cr})_{23}(\text{C},\text{B})_6$ phase from 5 to 33 nm and the $\eta\text{-Fe}_3\text{Mo}_3\text{C}$ carbide growing from 10 to 27 nm. In general, the $\eta\text{-Fe}_3\text{Mo}_3\text{C}$ carbide is 20% smaller than the $(\text{Fe,Cr})_{23}(\text{C},\text{B})_6$ one. The opposite behavior is observed for the χ -phase, which reduces its size at higher temperatures. XRD results are in agreement with the values measured from the STEM images, although explicit sizes cannot be addressed to a specific phase in this last case.

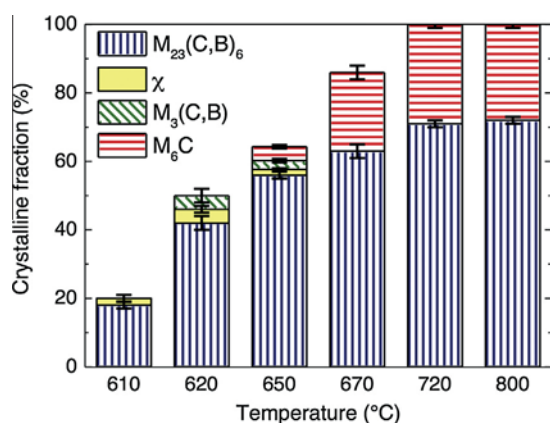


Fig. 4. Crystalline fraction of the χ -phase, $\text{M}_{23}(\text{C},\text{B})_6$, $\text{M}_3(\text{C},\text{B})$ and $\eta\text{-Fe}_3\text{Mo}_3\text{C}$ phases found by XRD as a function of the temperature. The missing sections at temperatures below 720 °C correspond to the amorphous phase.

The lattice parameters of the χ -phase remain almost unchanged, see Table 2. On the other hand, a slow and continuous decrease in the lattice parameters of the $(\text{Fe,Cr})_{23}(\text{C},\text{B})_6$ phase indicates the constant ejection of large elements such as Mo. A larger variation is observed in $\text{M}_3(\text{C},\text{B})$ and $\eta\text{-Fe}_3\text{Mo}_3\text{C}$, in which a faster increase of this large element in the carbide can explain the enlarged lattice parameters. These findings are correlated with the chemical data, obtained by APT, in the discussion section.

A general view of the APT reconstructions of the annealed alloys is presented in Fig. 5. The shown iso-concentration surfaces are set to highlight sub-volumes with the highest chemical gradients of the plotted elements. The atomic concentrations obtained from the mass spectra inside these regions and their chemical evolution as a function of the annealing temperature are plotted in Fig. 6. The sub-volumes of Fig. 5 can be linked with the phases identified by XRD and TEM by correlating their chemical composition with the typical stoichiometry of the corresponding phases. Thus, the different phases are identified in the figure by the isoconcentration surfaces plotted in different colors: yellow for the χ -phase, blue for $(\text{Fe,Cr})_{23}(\text{C},\text{B})_6$, purple for $\text{M}_3(\text{C},\text{B})$ and red for $\eta\text{-Fe}_3\text{Mo}_3\text{C}$. At the same time, the individual atoms are mapped as colored dots: green for Fe, blue for Cr and red for Mo. The lower images correspond to 1–3 nm thick virtual cross-sections of the cylindrical reconstructions that evidence the chemical partitioning.

In contrast to the homogeneous distribution within the as-quenched amorphous samples, annealing at 550 °C leads to the deviation of the statistical solute distribution from the calculated binomial distribution. The performed statistical analyses indicate chemical heterogeneity in the alloy. The most significant deviations were observed in the Fe and Cr elemental distributions with values of chi-square above 20. Despite this chemical redistribution, no signals of crystallization or cluster formation are evident, as can be observed in Fig. 5. At 620 °C localized FeCr-rich regions below 15 nm are formed. These regions correspond to the blue $(\text{Fe,Cr})_{23}(\text{C},\text{B})_6$ and the purple $\text{M}_3(\text{C},\text{B})$ borocarbides. Larger B-depleted regions, depicted in yellow, correspond to the χ -phase. The borocarbides grow in size and number and reject Mo atoms to the amorphous matrix. At 650 °C the $\eta\text{-Fe}_3\text{Mo}_3\text{C}$ crystalline phase emerges from the Mo-enriched regions. At 670 °C the χ -phase is no longer observed while the amorphous phase is only faintly noticeable. At the same temperature, regions corresponding to the composition of the $\text{M}_3(\text{C},\text{B})$ were still present in the APT reconstructions, even if this phase was no longer detected by XRD. At 720 °C and 800 °C only two types of regions are present, namely one enriched with Fe and Cr and the second one enriched with Mo, corresponding to the $(\text{Fe,Cr})_{23}(\text{C},\text{B})_6$ and the $\eta\text{-Fe}_3\text{Mo}_3\text{C}$ phases, respectively. At these temperatures no more traces of the amorphous phase are visible. An important observation is that after annealing at temperatures above 670 °C the corresponding FeCr-rich and Mo-rich phases appear

Table 2

Lattice parameters (in Å) calculated by the Rietveld method from the XRD patterns after annealing. Uncertainties on the last significant digit are given in parentheses.

Phase	610 °C	620 °C	650 °C	670 °C	720 °C	800 °C
χ (Fe,Cr) ₂₃ (C,B) ₆	9.083(5) 10.640(10)	9.091(3) 10.639(3)	9.090(1) 10.643(1)	– 10.621(3)	– 10.621(2)	– 10.613(1)
M ₃ (C,B)	–	5.070(3) 6.728(3)	5.198(3) 6.697(3)	–	–	–
η -Fe ₃ Mo ₃ C	–	4.315(3)	4.407(3) 11.017(7)	11.026(3)	11.055(3)	11.065(1)

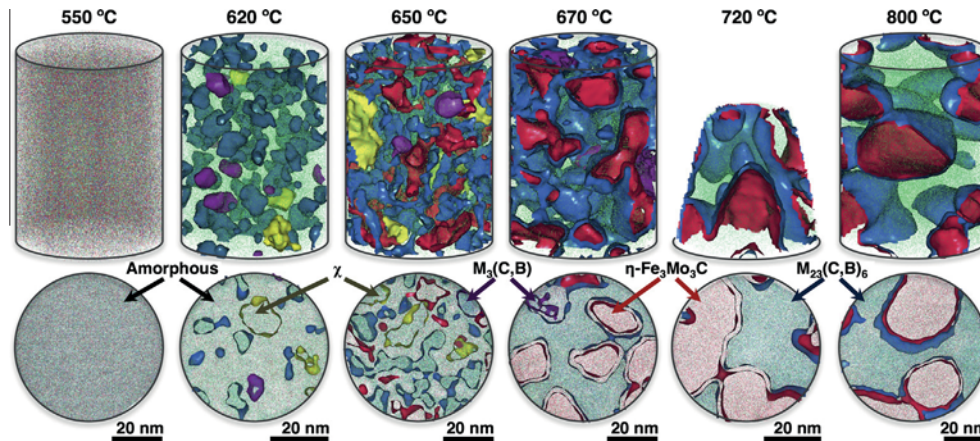


Fig. 5. Elemental distribution in APT reconstructions of the annealed alloys (Fe: green, Cr: blue, Mo: red). The lower images are virtual slices (1–3 nm) of the corresponding selected cylindrical regions. Iso-concentration surfaces highlight regions of highest elemental concentration. In yellow, the 1% B iso-concentration surface correspond to the χ -phase for the alloys annealed at 620 and 650 °C; in purple 40% CrC identifies M₃(C,B) at 620 and 650 °C while 39% CrC correspond to the alloy annealed at 670 °C. Blue iso-surfaces correspond to the (Fe,Cr)₂₃(C,B)₆ borocarbide at 63% FeCr for samples annealed at 620 and 650 °C, and 67% FeCr for higher temperatures. η -Fe₃Mo₃C is represented by red iso-surfaces of 28% Mo at 650 °C and 30% Mo for alloys annealed at higher temperature. (For interpretation of the references to color in this figure legend, the reader is referred to the web version of this article.)

in continuous topological arrangements, forming an interconnected network morphology, or in other words, a percolated microstructure.

Indications of a fifth phase were observed at 620 °C. Few spherical regions of less than 6 nm in size were isolated in terms of iso-concentration surfaces of 71% FeMo. The calculated composition was 59.4% Fe, 11.09% Cr, 16.90% Mo, 10.74% C and 1.43% B. Similar to the χ -phase these particles do not dissolve B in large concentrations but do dissolve a large amount of C; however, their Fe content is \sim 9% higher compared to the χ -phase. These regions could hence correspond either to a χ -phase with deviating stoichiometry or to α crystals that were also presumably identified by TEM.

The elemental evolution of the found crystallized phases as a function of the annealing temperature is plotted in Fig. 6. The composition of the χ -phase remains practically unchanged with the increase in temperature. By considering only the metallic elements (Fe 60.2%, Cr 18.1%, Mo 21.7%) this phase is close to the stoichiometry of the ternary intermetallic Fe₁₈Cr₆Mo₅ [32] although it dissolves large amount of C, close to the nominal composition of the as-quenched alloy (B is rejected and reduced below a value of 0.1%). The (Fe,Cr)₂₃(C,B)₆ borocarbide shows slight variations in composition where the most evident

one is a slow but continuous depletion of Mo as the temperature increases. The M₃(C,B) borocarbide shows a steep decrease in Cr with the consequent increase of Fe, C and Mo. Boron concentration remains almost steady at \sim 7%. Finally, η -Fe₃Mo₃C shows enrichment of Mo while C and Cr decrease their concentration in \sim 3% and 2%, respectively, in the temperature range of 650–800 °C. The solubility of B in this phase is limited and consequently decreased to a level below 2%.

Proximity histograms in Fig. 7 evidence pronounced chemical partitioning and phase boundary segregation of C and B [39]. More diffuse grain boundaries would be expected for the alloys crystallized at low temperatures, such as 620 and 650 °C as observed by TEM. For these lower temperatures the chemical gradients between the different phases are progressive and smooth with no accumulation or depletion of the elements at the interfaces, as exemplified for the M₂₃(C,B)₆/M₆C interface plotted at 650 °C (Fig. 7a). At higher temperatures these chemical gradients become sharper. However, while the temperature increases, C and B accumulate at the interface, as indicated by arrows for the plots at 670 °C and 800 °C (Fig. 7b and c, respectively). Carbon is also highlighted by purple iso-surfaces at 22% in the reconstruction at 800 °C (Fig. 7d). This C buildup is observed at temperatures above 670 °C and is

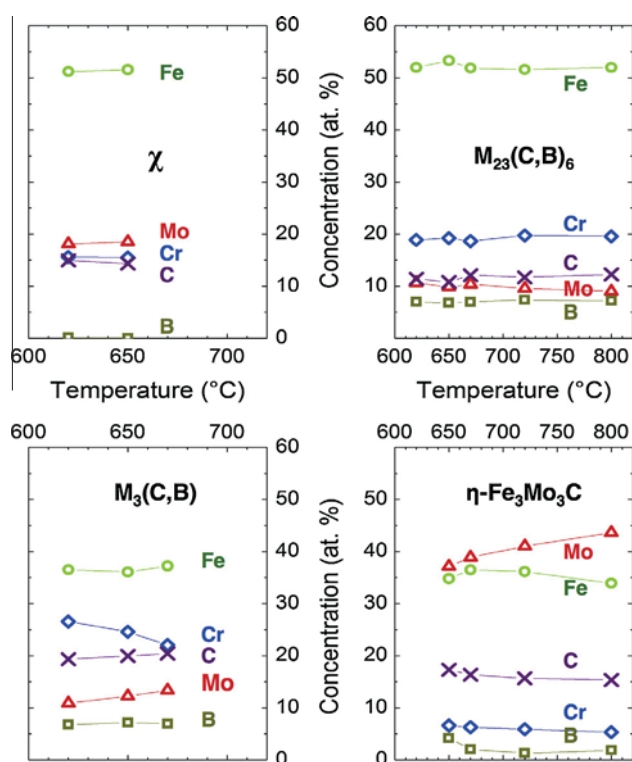


Fig. 6. Concentration evolution of the different regions determined by APT as a function of the annealing temperature.

not homogeneous over all interfaces, but localized only in a few regions and likely linked to the dissolution of the $M_3(C,B)$ phase.

3.2. Corrosion behavior

The microstructural changes described above were correlated to the corrosion behavior of the alloys. Fig. 8a shows linear sweep voltammetry tests in 0.1 M HCl solution. As shown by our group for a similar case [10], the results indicate a transition from a passive state limited by transpassive Cr dissolution to an earlier breakdown of the corrosion properties related to transpassive Mo dissolution, depending on the thermal history. The fully amorphous alloy shows a wide passive range with low current density (less than $50 \mu A cm^{-2}$) and a breakdown potential near $1.1 V_{SHE}$ comparable to that of pure Cr. Increasing the annealing temperature to $620^\circ C$ leads to a moderately larger passive current density and a more pronounced initial dissolution peak compared to the as-quenched material. The sample annealed at $650^\circ C$ presents a rather pseudopassive polarization curve with a breakdown potential near the fully amorphous state. This transition temperature reflects a severe detrimental effect on the corrosion behavior and is related to the formation of the first Mo-rich nanocrystals. As the annealing temperature further increases above $670^\circ C$, the polarization curves show an early material breakdown close to a potential of $0.3 V_{SHE}$, considerably lower than for the amorphous state, and the

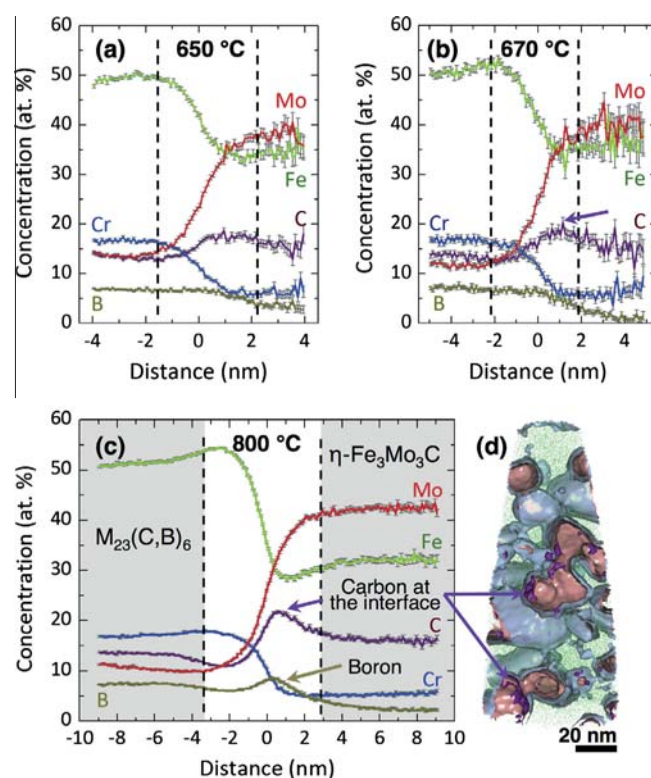


Fig. 7. Concentration profiles across $M_{23}(C,B)_6/M_6C$ interfaces at (a) 650, (b) 670 and (c) 800 °C. (d) Carbon isoconcentration surfaces (purple) at 22%, highlighting its accumulation at the $M_{23}(C,B)_6$ (blue)/ M_6C (red) interface in the APT reconstruction of the alloy annealed at 800 °C. (For interpretation of the references to color in this figure legend, the reader is referred to the web version of this article.)

corrosion current curve closely resembles the behavior of pure Mo.

To analyze the corrosion effects close to the breakdown potential, galvanic polarization tests were carried out for 2000 s in 0.1 M HCl. At $620^\circ C$ a homogeneous, only partially rough, passive surface is observed in the SEM image of the respective cross-section in Fig. 8b. White dashed lines indicate the limit between the original surface and the redeposited material during the cutting process. Etch cavities develop on the surface at $650^\circ C$ in the Mo-depleted regions with small penetration into the bulk material (Fig. 8c). The chemical stability is compromised when Cr is depleted in the percolating Mo-rich phase (Fig. 8d at $800^\circ C$). Selective dissolution can be then sustained originating mesoporosity.

4. Discussion

The combination of the state-of-the-art analysis obtained by APT and high resolution TEM, together with the quantitative analysis performed by XRD, enables presenting a coherent atomic-scale picture of the crystallization and phase evolution of different regions during annealing. On the other hand, subtle chemical variations, important for corrosion or mechanical performance, can

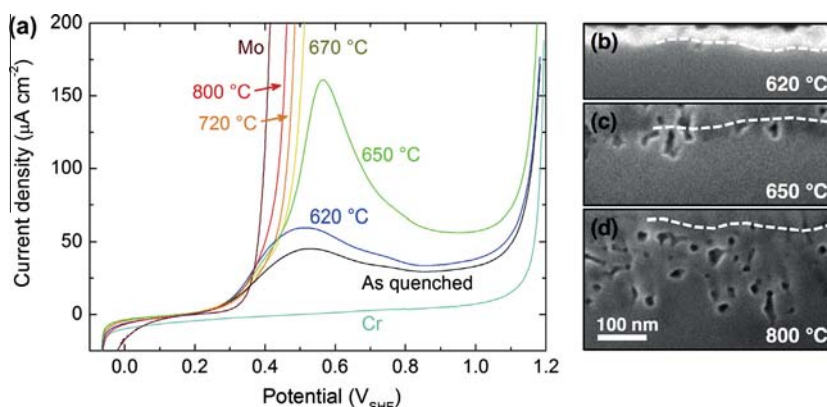


Fig. 8. (a) Potentiodynamic polarization curves of the amorphous, partially and fully nanocrystalline states of $\text{Fe}_{50}\text{Cr}_{15}\text{Mo}_{14}\text{C}_{15}\text{B}_6$ compared to pure Cr and Mo in aerated 0.1 M HCl (with a scan rate of 2 mV s^{-1}) [10]. Potentials are referred to as SHE. (b) SEM images of the cross-section after potentiostatic polarization close to the breakdown potential during 2000 s for the sample annealed for 20 min at 620 °C (c) 650 °C and (d) 800 °C. White dashed lines indicate the limit between the original surface and the redeposited milled material.

often not be well captured by energy dispersive X-ray spectroscopy (EDX) analyses alone but have to be aided by APT analysis.

Devitrification of the studied alloy occurs in a multistep process with the primary crystallization of a Fe–Cr–Mo ternary intermetallic, often referred as τ_1 [32] or χ phase [33] and a $\text{M}_{23}(\text{C,B})_6$ borocarbide. Crystallization studies of Fe–Cr–Mo metallic glasses often report the presence of α -Fe during the first stages of crystallization [40–42]. In our study, we provide evidence by both TEM and APT of a bcc structure consisting of 59.4% Fe, 11.1% Cr, 16.9% Mo with additional C dissolved in $\sim 10.7\%$. However, this structure cannot be unambiguously assigned to the ordered intermetallic χ -phase by XRD since the superlattice reflections were not distinguished from the background in the patterns. As this phase has a mass fraction lower than 11% and the superlattice diffraction peaks have low intensity and may overlap with other second phase peaks, it is difficult to distinguish it by conventional XRD. This bcc solid solution (α -Fe type or ordered intermetallic χ -phase) was not detected in samples annealed at a temperature of 650 °C or higher. This could indicate that either it had partially dissolved and hence could not be detected in the small volume probed by APT, or it had completely vanished.

The chemical stoichiometry obtained by APT mass spectra and TEM diffraction analyses confirmed the presence of the intermetallic χ -phase instead of an α -Fe type solid solution. The χ -phase appears as an intermediate ternary phase ($\text{Fe}_{60.3}\text{Cr}_{18.2}\text{Mo}_{21.5}$) with a large solubility of C ($\sim 14.5\%$), while the solubility of B is negligible. The lattice parameter of this phase expands from the reported values of the pure ternary intermetallic (8.89 Å) to ~ 9.083 Å after its formation, related to the large amount of interstitial C atoms. A modest further increase to 9.104 Å close to its decomposition was associated to the small rise in Mo and Fe content. Metastable χ phases usually form in Mo containing Fe–Cr alloys, such as duplex stainless steels [43,44]. From

a mechanical perspective the χ -phase is undesired since it is a brittle intermetallic that nucleates at grain boundaries during aging. This leads to a reduction in ductility, toughness and intergranular corrosion resistance due to a sensitization effect. As in our case, the χ -phase may nucleate at relatively low temperatures (below 610 °C) and is subsequently dissolved/transformed into a secondary phase (above 670 °C). The higher amount of Mo in this phase compared to the amorphous matrix may suggest that the chemical contrast observed in the dark field STEM image at 550 °C (Fig. 2) could be related to nucleation sites for the χ -phase.

$\text{M}_{23}(\text{C,B})_6$ is formed at the expense of the amorphous matrix also at the lower annealing temperatures and remains stable until full crystallization. This borocarbide corresponds to the majority phase by comprising 71–76% of the crystallized fraction at all studied temperatures. At 800 °C this phase contains 52.0% Fe, 19.6% Cr, 9.0% Mo, 12.2% C and 7.2% B. A small progressive decrease in the lattice parameter, from 10.640 Å at 610 °C to 10.613 Å at 800 °C, is related to the slow rejection rate of 1.6% of Mo atoms from the structure as the temperature rises. The grain size increases about eight times from its formation at 610 °C until full crystallization at 800 °C. However, as the samples were kept for 20 min in the furnace and were not quenched afterwards to retain the microstructure, kinetic effects were then not considered and specific tests are necessary to assess the diffusional aspects of crystallization, grain growth and further coarsening.

The intermediate $\text{M}_3(\text{C,B})$ borocarbide crystallizes at a few degrees above, i.e. at 620 °C. Its composition after formation (36.5% Fe, 26.5% Cr, 10.9% Mo, 19.3% C and 6.8% B) is highly unstable and changes continuously with temperature. $\text{M}_3(\text{C,B})$ nucleates independently from the other phases, and from the APT reconstructions of the samples annealed at 670 °C it seems to consume the remaining amorphous phase, where it coexist with the $\text{M}_{23}(\text{C,B})_6$ and the later formed η - $\text{Fe}_3\text{Mo}_3\text{C}$ phases (see Fig. 5). An

interface controlled transformation may explain the steep reduction of Cr (4.5%) between 620 and 670 °C, as this element would gradually become scarcer in the amorphous matrix. In a similar way, the increase in C (1.1%) and Mo (2.5%) would be related to the enrichment of these elements in the amorphous matrix while the other initially crystallized phases grow. Above 670 °C the $M_3(C,B)$ phase decomposes. APT reconstructions at this temperature show narrowed $M_3(C,B)$ grains between the $M_{23}(C,B)_6$ ones, which suggests that $M_3(C,B)$ dissolves or transforms into $M_{23}(C,B)_6$. Additionally, a similar Cr content is observed in the two phases at 670 °C. The 9% excess of C atoms in $M_3(C,B)$ compared to $M_{23}(C,B)_6$ then would remain at the grain boundaries, explaining the increasing amount of C in the $M_{23}(C,B)_6/M_6C$ interfaces after annealing above 670 °C (Fig. 7) and the Mo excess would diffuse towards the $\eta\text{-Fe}_3\text{Mo}_3\text{C}$ phase particles.

The χ -phase begins to decompose at the same temperature as $\eta\text{-Fe}_3\text{Mo}_3\text{C}$ appears, namely, at ~ 650 °C. The continuous rejection of Mo from the $M_3(C,B)$ and the formation of the dominant $M_{23}(C,B)_6$ phase both favor the formation of this Mo-rich phase, which is stable also in similar systems although not always easy to identify [40]. At 800 °C this phase contains 33.9% Fe, 43.6% Mo, 5.3% Cr, 15.4% C and 1.8% B. Interface diffusion processes lead to a change in the phase composition and $\eta\text{-Fe}_3\text{Mo}_3\text{C}$ rapidly consumes the remaining Mo in the amorphous as well as the transformed $M_3(C,B)$. The significant increase of Mo from 37.1% to 43.9% enlarges the lattice parameter gradually from 11.017 to 11.065 Å in the 650–800 °C temperature range.

The knowledge of the microstructural and chemical information is essential to better understand the performance of the material under specific conditions. Amorphous Fe-based alloys containing more than 6% Cr, as in the case studied here, usually show good corrosion behavior [5]. This is often attributed to the high degree of chemical homogeneity of amorphous alloys, i.e. to a lack of defects and decorated grain boundaries which can act as local elements. The structural and chemical homogeneity of the amorphous phase provides a high amount of passivating elements for the formation of a homogeneous film of chromium oxides and oxihydroxides [5,45]. As the alloy starts to crystallize Cr-depleted regions form due to partitioning, and these zones are preferentially attacked by corrosion owing to a lack in passivation, as shown in our previous study [10]. With a crystalline fraction below 50% (i.e. 620 °C in the studied system) this preferential dissolution leads to a nano-scale roughness of the surface, including Cr-rich crystallites. The respective passive oxide, therefore, needs to overgrow a structurally inhomogeneous substrate. Yet the created rough, partially nano-crystalline surface shows nearly identical breakdown and passive behavior as the amorphous state with an only slightly increased passive current density. The heterogeneous structure has a detrimental effect on the corrosion resistance with advanced partitioning phenomena. The phase

separation and crystallization causes formation of Mo-rich zones with Cr in quantities below 6.5%, which will dissolve preferentially. The dissolution process can be blocked in partially crystallized alloys (i.e. 650 °C) by the remaining amorphous phase, small crystal sizes and the lack of phase percolation. However, a percolated morphology, as observed at crystallized volume fractions above 80%, enables finally the dissolution throughout the material causing early breakdown of the corrosion resistance. The sensitization process, often responsible for intergranular corrosion, is not observed in this case. Cr-depleted regions are here due to the formation of the stable $\eta\text{-Fe}_3\text{Mo}_3\text{C}$ phase and not related to the formation of Cr-rich carbides with Cr-depletion at the grain boundaries. Nonetheless, it is worth mentioning the much larger amount of C and B considered in our system compared to conventional corrosion resistant steels where sensitization may play an important role. Finally, the preferential dissolution of the $\eta\text{-Fe}_3\text{Mo}_3\text{C}$ phase can be sustained by static polarization generating the formation of mesoporous structures of Fe,Cr-rich carbides with potential applications, for example, in the field catalysis where a large surface-to-volume ratio is required. The resulting morphology is similar to the nanoporous structures obtained by classical dealloying e.g. of noble metal alloys [46,47] but the process is a selective dissolution of a pre-existing nanoscale dual-phase structure [48].

5. Conclusions

The microstructural and detailed chemical changes related to the crystallization and further phase evolution of the $\text{Fe}_{50}\text{Cr}_{15}\text{Mo}_{14}\text{C}_{15}\text{B}_6$ amorphous steel were followed by XRD-Rietveld, TEM and APT analyses accounting for microstructural and chemical details. Crystallization occurs in a multistep process with the primary crystallization of an intermetallic corresponding to the χ -phase and a stable $M_{23}(C,B)_6$ borocarbide. The χ -phase and a later formed $M_3(C,B)$ are intermediate phases that dissolve above 650 °C. At the same temperature an $\eta\text{-Fe}_3\text{Mo}_3\text{C}$ carbide appears. The transformation of the χ -phase into the $\eta\text{-Fe}_3\text{Mo}_3\text{C}$ and the dissolution of the $M_3(C,B)$ to form part of the $M_{23}(C,B)_6$ phase are suggested. The final microstructure consist of a dual-phase, $M_{23}(C,B)_6/\eta\text{-Fe}_3\text{Mo}_3\text{C}$, percolated nanostructure (30–50 nm grain size) with a phase ratio 7:3 respectively. The changes on the elemental composition of all the observed phases are also correlated with their crystal lattice parameters. Devitrification was induced by thermal annealing for 20 min and therefore kinetic parameters were not taken into account in this study. Further analyses to establish the crystallization kinetics, nucleation and growth are advised to complement the phase development presented here.

The corrosion properties were analyzed and interpreted on the basis of the observed microstructures. The initial crystallization of the Cr-rich phases: χ , $M_{23}(C,B)_6$ and $M_3(C,B)$, does not cause a severe deterioration of the

corrosion behavior. The later formation of the η -Fe₃Mo₃C phase with less than 6% Cr sets a transition from a passive behavior to transpassive Mo dissolution when at least 80% of the alloy has crystallized. Selective dissolution of the Mo-rich phase can be then sustained to form mesoporous structures rich in Cr, Fe and C.

Acknowledgements

We acknowledge K.J.J. Mayrhofer and S.O. Klemm for assistance in the electrochemical analyses. M.J.D. and D.C. acknowledge financial support from CICYT Grant MAT2010-14907 and Generalitat de Catalunya, Spain, 2009SGR01225 and 2009SGR01251. F.U.R. acknowledges support by DAAD Acciones Integradas Hispano – Alemanas PPP 0811941.

References

- [1] Eckert J, Mattern N, Zinkevitch M, Seidel M. *Mater Trans JIM* 1998;39:623.
- [2] Torrens-Serra J, Bruna P, Stoica M, Roth S, Eckert J. *J Non-Cryst Solids* 2013;367:30.
- [3] Schuh CA, Hufnagel TC, Ramamurty U. *Acta Mater* 2007;55:4067.
- [4] McHenry ME, Willard MA, Laughlin DE. *Prog Mater Sci* 1999;44:291.
- [5] Hashimoto K. *Appl Surf Sci* 2011;257:8141.
- [6] Yoshisawa Y, Oguma S, Yamauchi J. *J Appl Phys* 1988;64:6044.
- [7] Kojima A, Horikiri H, Kamamura Y, Makino A, Inoue A, Matsumoto T. *Mater Sci Eng* 1994;A179/A180:511.
- [8] Iwanabe H, Lu B, McHenry ME, Laughlin DE. *J Appl Phys* 1999;85B:4424.
- [9] Lewandowski JJ, Wang WH, Greer AL. *Philos Mag Lett* 2005;85:77.
- [10] Duarte MJ, Klemm J, Klemm SO, Mayrhofer KJJ, Stratmann M, Borodin S, et al. *Science* 2013;341:372.
- [11] Tiberto P, Baricco M, Olivetti E, Piccin R. *Adv Eng Mater* 2007;9:468.
- [12] Pardo A, Merino MC, Otero E, Lopez MD, M'hich A. *J Non-Cryst Solids* 2006;352:3179.
- [13] Inoue A, Takeuchi A. *Acta Mater* 2011;59:2243.
- [14] Stoica M, Kumar S, Roth S, Ram S, Eckert J, Vaughan G, et al. *J Alloys Compd* 2009;483:632.
- [15] Inoue A, Baolong S, Koshiba H, Kato H, Yavari AR. *Nat Mater* 2003;2:661.
- [16] Hashimoto K. *Corrosion* 2002;58:715.
- [17] Li H, Yi S. *Mater Sci Eng A* 2007;449–451:189.
- [18] Miller MK, Kelly TF, Rajan K, Ringer SP. *Mater Today* 2012;15:158.
- [19] Seidman DN. *Annu Rev Mater Res* 2007;37:127.
- [20] Marquis EA, Choi PP, Danoix F, Kruska K, Lozano-Perez S, Ponge D, et al. *Microsc Today* 2012;20:44.
- [21] Raabe D, Choi PP, Li YJ, Kostka A, Sauvage X, Lecouturier F, et al. *MRS Bull* 2010;35:982.
- [22] Chen YZ, Herz A, Li YJ, Borchers C, Choi P, Raabe D, et al. *Acta Mater* 2013;61:3172.
- [23] Raabe D, Sandlöbes S, Millán J, Ponge D, Assadi H, Herbig M, et al. *Acta Mater* 2013;61:6132.
- [24] Liddicoat PV, Liao XZ, Zhao Y, Zhu Y, Murashkin Y, Lavernia EJ. *Nat Commun* 2010;1:63.
- [25] Ponambalam V, Poon SJ, Shiflet GJ. *J Mater Res* 2004;19:1320.
- [26] Liebermann HH, Graham CD. *IEEE Trans Magn* 1976;12:921.
- [27] Greer AL. *Science* 1995;267:1947.
- [28] Lutterotti L, Ceccato R, Dal Maschio R, Pagani E. *Mater Sci Forum* 1998;278–281:87.
- [29] Bolera ML, Pradelli G. *Metall Ital* 1971;63:107.
- [30] Alconchel S, Sapiña F, Martínez E. *Dalton Trans* 2004:2463–8.
- [31] Medvedeva NI, Shein IR, Gutina YO, Ivanovskii AL. *Phys Solid State* 2007;49:2298.
- [32] Kroupa A. Ternary alloy systems, Landolt–Börnstein – group IV physical chemistry, vol. 11D3. Berlin: Springer Verlag; 2008. p. 157.
- [33] Anderson JO, Lange N. *Metall Trans A* 1988;19A:1385.
- [34] Kaspar JS. *Acta Metall* 1954;2:456.
- [35] Thompson K, Lawrence D, Larson DJ, Olson JD, Kelly TF, Gorman B. *Ultramicroscopy* 2007;107:131.
- [36] Miller MK, Russell KF, Thompson GB. *Ultramicroscopy* 2005;102:287.
- [37] Hellman O, Vandenbroucke J, Rusing J, Isheim D, Seidman D. *Microsc Microanal* 2000;6:437.
- [38] Klemm SO, Schauer JC, Schuhmacher B, Hassel AW. *Electrochim Acta* 2011;56:4315.
- [39] Tytko D, Choi PP, Klöwer J, Kostka A, Inden G, Raabe D. *Acta Mater* 2012;60:1731.
- [40] Sidique M, Iqbal M, Akhter JI, Ahmad M. *J Alloys Compd* 2009;482:L25.
- [41] Iqbal M, Akhter JI, Zhang HF, Hu ZQ. *J Non-Cryst Solids* 2008;354:3284.
- [42] Ha HM, Payer JH. *Met Mater Trans A* 2009;40A:2519.
- [43] Michalska J, Sozanska M. *Mater Charact* 2006;56:355.
- [44] Xu W, San Martin D, Rivera Diaz del Castillo PEJ, van der Zwaag S. *Mater Sci Eng A* 2007;467:24.
- [45] Pang S, Zhang T, Asami K, Inoue A. *Mater Trans* 2002;43:2137.
- [46] Renner FU, Stierle A, Dosch H, Kolb DM, Lee TL, Zegenhagen J. *Nature* 2006;439:707.
- [47] Ankah GN, Pareek A, Rohwerder M, Renner FU. *Electrochim Acta* 2012;85:384.
- [48] Jayaraj J, Park JM, Gostin PF, Fleury E, Gebert A, Schultz L. *Intermetallics* 2009;17(12):1120–3.